Multi-scale designed Zeolitic Imidazolate Framework−derived N-doped cobalt/carbon composites with enhanced electromagnetic performance by magnetic-dielectric synergy

Yao Xiang[1,4] · Jiahang Qiu[1,4] · Eman Ramadan Elsharkawy[2] · Saad Melhi[3] · Mu Zhang[1,4] · Zhengtang Luo[5] · Rongzhi Zhao[6] · Xudong Sun[1,4]

Abstract

The pursuit of achieving wideband electromagnetic wave absorption to meet the demands in multiple fields has attracted attention in the field of electromagnetic wave absorption. Considering that the dipole moments of different scales can correspond to different polarization bands, the coupling of multi-scale loss mechanisms may help to realize the electromagnetic wave absorption in the wide band. Therefore, we fabricated N-doped Co/C composites derived from ZIF-67 through a facile wet chemistry approach and pyrolysis process. Due to the precise fabrication method and the design of the Stranski-Krastanow growth mode, the prepared N-doped Co/C composites contain abundant functional groups, magnetic particles, and cobalt quantum dots. By combining atomic-scale doping loss and mesoscopic-scale hollow structures, the Co/C composite materials achieve the coupling of multiple-scale loss mechanisms and demonstrate outstanding electromagnetic wave absorption performance: the minimum reflection loss (RL_{min}) value reaches −57.0 dB at 17.9 GHz when the thickness is 1.73 mm, and the effective absorption bandwidth (EABD) reaches the maximum value of 5.7 GHz when the thickness is 2 mm. To sum up, this work provides a new strategy for realizing the broadband absorption of further electromagnetic wave absorption materials.

Keywords ZIF-67 · Co/C composites · Multiple-scale loss mechanisms · Microwave absorption

1 Introduction

Due to the explosive development of electromagnetic wave utilization in the information age, the electromagnetic wave (EMW) pollution caused by radiofrequency electromagnetic radiation has become impossible to ignore due to its impact on human health and the operation of precision equipment [1, 2]. Therefore, electromagnetic interference shielding materials and electromagnetic wave absorbing materials (MAMs) have attracted much attention as the main electromagnetic functional materials to deal with electromagnetic pollution problems [3, 4]. As electromagnetic pollution

Yao Xiang and Jiahang Qiu contributed equally to this work.

✉ Mu Zhang
zhangm@mail.neu.edu.cn

✉ Xudong Sun
xdsun@mail.neu.edu.cn

1 Key Laboratory for Anisotropy and Texture of Materials (Ministry of Education), School of Materials Science and Engineering, Northeastern University, Shenyang 110819, People's Republic of China

2 Department of Chemistry, Faculty of Science, Northern Border University, Arar, Saudi Arabia

3 Department of Chemistry, College of Science, University of Bisha, Bisha 61922, Saudi Arabia

4 Foshan Graduate School of Innovation of Northeastern University, Foshan 528311, People's Republic of China

5 Department of Chemical and Biological Engineering, the Hong Kong University of Science and Technology, Clear Water Bay, Kowloon, Hong Kong 999077, People's Republic of China

6 Institute of Advanced Magnetic Materials, College of Materials and Environmental Engineering, Hangzhou Dianzi University, Hangzhou 310012, People's Republic of China

intensifies, researchers are increasingly troubled by the narrow absorption frequency band in MAMs [5]. In terms of this issue, since the dipole polarization losses at different scales correspond to different absorption bands, the coupling of multi-scale loss mechanisms is considered to be an effective solution to the narrow absorption bandwidth [6, 7].

Based on this rationale, metal-organic framework (MOF)–derived composites are considered reliable research subjects. Due to their programmable topological structures, MOFs often exhibit distinctive microscale morphologies, contributing to the EMW attenuation mechanisms at the mesoscale [8–10]. For instance, one-dimensional MIL-88 A nanorods [11] and two-dimensional CuBDC MOF nanosheets [12], owing to their unique stacking characteristics, can construct a three-dimensional conductive network at the mesoscale, thereby reducing the energy barriers for electronic migration and enhancing the composites' conductive loss capacity [13]. On the other hand, the presence of heteroatoms such as N and O in the organic framework of the precursor leads to the random distribution of heteroatoms in the thermally treated carbon matrix. These heterogeneous atomic sites induce the separation of local charge centers between the heteroatoms and carbon atoms, resulting in the emergence of polarized centers, which contribute to atomic-scale dipole moment polarization under the applied electromagnetic field [14–16]. Unfortunately, the application of MOF materials often requires high-temperature pyrolysis, which results in the composites being unable to maintain the morphology of the precursor, leading to collapse or agglomeration. Additionally, the inevitable aggregation and growth of magnetic particles after pyrolysis also pose challenges to the EMW absorption performance due to the skin-effect phenomenon. Previous studies have indicated that incorporating conductive pathways into the MOF structure can effectively avert the defects caused by pyrolysis [17]. However, this approach also leads to the loss of magnetic loss. Therefore, the key focus lies in finding strategies to preserve the existing advantages of MOF while avoiding the drawbacks introduced by pyrolysis, thereby achieving the coupling of multi-scale loss mechanisms.

To address these issues, a viable approach is to optimize suitable MOF materials. Among these materials, Zeolitic Imidazolate Frameworks (ZIFs) have garnered considerable attention due to their unique metal-N coordination and diverse lattice structures. These characteristics inherently prevent the aggregation of magnetic particles and enable the realization of multiple microscale morphologies [18–21]. Therefore, achieving the coupling of multi-scale loss mechanisms through the optimization of ZIFs has naturally become a focal point of research. For instance, Zhang and his group have achieved the uniform distribution of Fe single atoms on a carbon matrix by incorporating Fe phthalocyanine into ZIF-8, which facilitated dipolar polarization loss at the atomic scale and harnessed the magnetic loss capabilities contributed by Fe_3O_4 clusters. Remarkably, the as-synthesized composites achieved a minimum reflection loss (RL_{min}) of −64.75 dB at a thickness of 2.7 mm [22]. In addition, other research approaches based on ZIF modifications, such as ZIF-67@LDH [23], Fe_3O_4@ZIF-8 [24], and Zn/Co ZIF-L [25], have also made significant contributions in this research field. Inspired by these studies, integrating ZIFs with materials showcasing diverse loss mechanisms and achieving a multi-size distribution of magnetic particles could enable the coupling of multi-scale loss mechanisms while retaining the inherent advantages of ZIFs.

In this paper, ZIF-67 is utilized as an internal template with coating a phenol-formaldehyde resin (PR) synthesized from resorcinol and formaldehyde onto the surface to form a core-shell structure. Owing to the decomposition and renucleation of the layered cobalt hydroxide generated under alkaline conditions in the PR shell based on the Stranski-Krastanow mode, as well as the carbonization of ZIF-67, a multi-sized distribution of magnetic particles has been achieved, which coupled with functional group polarization and polarization of heteroatoms in the carbon matrix, and has led to the coupling of multi-scale loss mechanisms, resulting in excellent EMW absorption performance: a minimum reflection loss (RL) value of −57.0 dB within a thickness of 1.73 mm and a maximum effective absorption bandwidth (EABD) of 5.7 GHz within a thickness of 2 mm. Therefore, in order to solve the problem of a narrow absorption band, this work realizes the coupling of a multi-scale loss mechanism, which provides a new strategy for the design of high-performance EMW absorption materials.

2 Result and discussion

The fabrication strategy of pomegranate-like [Co/NC]@NC is depicted in Fig. 1a. ZIF-67 nanoparticles were prepared by mixing cobalt nitrate hexahydrate and dimethylimidazole in methanol, and then aged for 24 h. Afterward, the ZIF-67 dispersion was added to an alkaline alcohol-water mixture, and an appropriate amount of resorcinol and formaldehyde was introduced. The mixture was stirred for 12 h to coat the ZIF-67 nanoparticles with phenol-formaldehyde resin. Finally, the ZIF-67@RF nanoparticles were carbonized under argon protection to obtain [Co/NC]@NC.

During the synthesis of the PR shell, the alkaline environment in the suspension causes the Co^{2+} adsorbed on the ZIF-67 surface to first combine with hydroxide ions to form layered cobalt hydroxide, which is then coated with PR shell, forming a laminar structure of $Co(OH)_2$@PR. We propose a hypothesis herein based on the Stranski-Krastanow growth mode to explain the arisen of cobalt quantum dots (CQDs) with sizes approximately around 5 nm (Fig. 1b). During the

Fig. 1 **a** Schematic illustration of the formation process of [Co/NC]@NC-T; **b** schematic illustration of the formation of CQDs in the Stranski-Krastanow mode
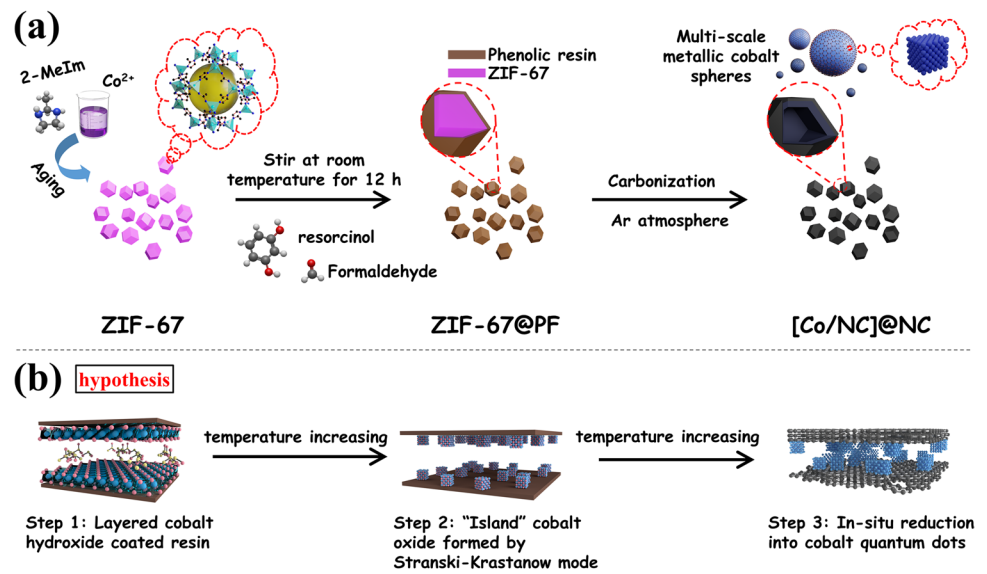
pyrolysis process, layered cobalt hydroxide with a hydrotalcite-like crystal structure undergoes decomposition and re-nucleation, whereafter forming island nucleation sites under the stress exerted by the encapsulating PR shell and finally growing into CQDs embedded within the carbon matrix [26–28].

The phase composition of the products at different preparation steps was characterized by X-ray diffraction (XRD) patterns as shown in Fig. S1 (Supporting Information) and

Fig. 2a. Figure S1 (Supporting Information) displays a series of diffraction peaks of both as-synthesized ZIF-67 and ZIF-67@PR, consistent with the crystallographic information reported in the literature, which confirms the successful synthesis of high-purity ZIF-67 [29]. Additionally, the XRD pattern of ZIF-67@PR displayed no characteristic diffraction peaks of phenol-formaldehyde resin, indicating that the phenol-formaldehyde resin layer coated on the ZIF-67 surface exists in an amorphous form. On the other hand,
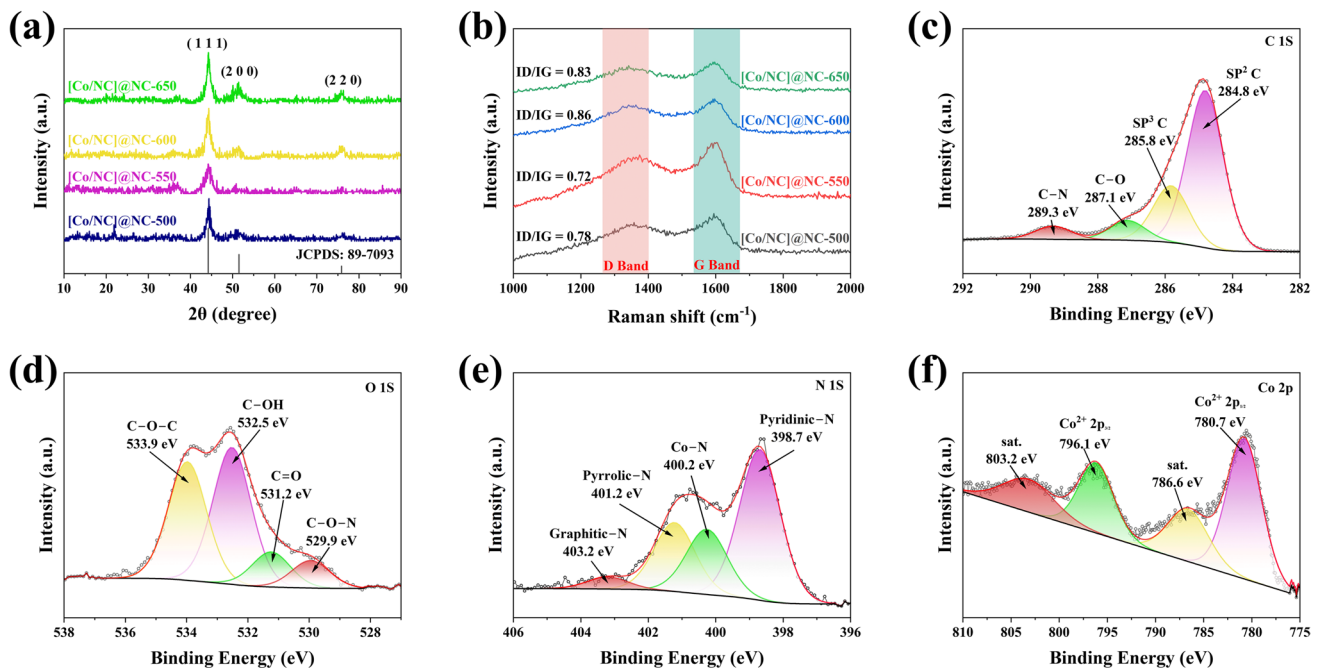

Fig. 2 **a** XRD patterns of [Co/NC]@NC-T; **b** Raman spectra of [Co/NC]@NC-T; XPS spectra of the [Co/NC]@NC-600: **c** C 1s region, **d** O 1s region, **e** N 1s region, **f** Co 2p region

the XRD patterns of [Co/NC]@NC-T ($T=500$, 550, 600, 650) obtained by carbonization at different temperatures are shown in Fig. 2a. All samples exhibit significant diffraction peaks corresponding to the face-centered cubic (FCC) structure. By comparing the diffraction patterns with the standard PDF card of FCC metallic cobalt (JCPDS NO. 89-7093), three characteristic diffraction peaks are identified in order of increasing 2θ angles as (111), (200), and (220) crystallographic planes. Therefore, it can be preliminarily concluded that the product is [Co/NC]@NC nanoparticles.

The [Co/NC]@NC samples obtained by pyrolysis at different temperatures were characterized by Raman spectroscopy, and the spectra are shown in Fig. 2b. For the Raman spectra of carbon-containing samples, the D band vibration peak at 1370 cm^{-1} and the G band vibration peak at 1589 cm^{-1} respectively represent the degree of disorder and order of carbon. Therefore, I_D/I_G can be used to represent the degree of order of carbon materials, that is, the degree of graphitization. The smaller the value of I_D/I_G, the higher the degree of graphitization [30–33]. From the spectra analysis, it can be observed that with the increase in carbonization temperature, the I_D/I_G values of [Co/NC]@NC-500 and [Co/NC]@NC-550 decrease from 0.78 to 0.72. Similarly, the I_D/I_G values of [Co/NC]@NC-600 and [Co/NC]@NC-650 decrease from 0.86 to 0.83. These reductions indicate an enhanced degree of graphitization in the carbon layer. Meanwhile, it is worth noting that samples between 550 and 600 °C exhibit a sharp increase in the I_D/I_G ratio. This phenomenon could be attributed to two reasons: (1) the anomalous growth of metallic cobalt grains within the sample at a carbonization temperature of 600 °C. The presence of larger cobalt particles reduces the specific surface area of the cobalt catalyst, resulting in a decrease in the proportion of amorphous carbon directly in contact with the cobalt particles, leading to a reduction in the production of graphite. Consequently, the I_D/I_G ratio increases from 0.72 to 0.86, which could be further supported by the subsequent transmission electron microscopy (TEM) images. (2) At temperatures equal to or below 550 °C during pyrolysis, a significant amount of uncarbonized organic compounds is retained in the sample, rendering the I_D/I_G values inadequate for accurately representing the graphite and carbon content. This assertion can be further supported by subsequent ε" curves.

X-ray photoelectron spectroscopy (XPS) was used to study the surface composition and valence states of the [Co/NC]@NC-600 (Fig. S2, Supporting Information and Fig. 2c–f). The survey spectra as displayed in Fig. S2 reveal the co-existence of C 1s, O 1s, N 1s, and Co 2p species. The C 1s spectra shown in Fig. 2c display four distinct peaks located at 284.8, 285.8, 287.1, and 289.3 eV, respectively, which can be indexed to the C–C sp2, C–C sp3, C–O, and C–N band [34]. Notably, the appearance of the C–O bond and C–N bond indicates that N and O atoms may enter the carbon six-membered ring as heteroatoms, contributing to the dipole moment polarization of the atoms. Similarly, the N 1s spectra shown in Fig. 2e can be divided into pyridinic N (398.7 eV), pyrrolic N (401.2 eV), and graphite N (403.2 eV), which also indicates that nitrogen has been doped into the carbon component derived from the ligand. Interestingly, there is also a distinct peak located at 400.2 eV in the N 1s spectra that can be attributed to the presence of Co–N, indicating that neither ZIF nor PR is fully pyrolyzed at this temperature [35]. In addition, as shown in Fig. 2d, the spectrum of O 1s can be divided into C–OH (532.5 eV), C–O–C (533.9 eV), C=O (531.2 eV), and C–O–N (529.9 eV). The presence of these chemical bonds is also further evidence of incomplete cleavage of the organic framework and the presence of numerous oxygen-containing functional groups in the carbon matrix. What is more, for the Co 2p spectrum, two kinds of peaks are observed which can correspond to Co^{2+} and satellite (Sat.). The peaks at 780.7 and 796.1 eV can correspond to Co^{2+} 2p3/2 and Co^{2+} 2p1/2, respectively, and the peaks at 786.6 and 803.2 eV can be attributed to shakeup satellite peaks, respectively.

The thermogravimetric (TG) curves show the weight variations of the samples from room temperature to 800 °C in the air (Fig. S3, Supporting Information). The metallic Co and CoO in composites were oxidized into Co_3O_4 through this process, and thus, the Co content in samples can be estimated according to the weight of the remanent material. By the mean of the calculation method, the Co contents of [Co/NC]@NC-600 are 40.0wt%. The N_2 adsorption-desorption isotherms and the corresponding Barrett-Joyner-Halenda (BJH) pore size distribution of the synthesized [Co/NC]@NC-T composite are exhibited in Fig. S4 (Supporting Information); the isotherms of all the samples showed a similar curve to the type IV isotherms with H4 hysteresis loop, which indicated the presence of mesopores and macropores with irregular distributions in the samples [36, 37]. The results show that samples possess relatively large specific surface areas, with abundant pore structures distributed both inside and outside of the samples, which contributes to a certain degree of enhancement in EMW absorption performance.

To further verify the incomplete decomposition of organic and the presence of functional groups, the [Co/NC]@NC-600 sample was characterized by Fourier transform infrared spectroscopy (FT-IR) (Fig. S5, Supporting Information). It can be found that there are multiple vibration peaks in the FT-IR spectra of the sample, among which the vibration peaks at 3440 cm^{-1} and 571 cm^{-1} belong to the tensile vibration of the hydroxyl group in adsorbed water and the stretching vibration of Co–O bond, respectively. In addition, other vibration peaks are caused by organic. Among them, the vibration peak located at 1574 cm^{-1} can be attributed to the stretching vibration of C=N in ZIF-67, while the

wide peak located at 1136–1306 cm^{-1} can be attributed to the imidazole ring vibration, which means that these two vibration peaks are from the incomplete decomposition of ZIF-67 [38]. Correspondingly, of the remaining peaks attributed to the PR, the vibrational peaks at 650 cm^{-1} could be attributed to the hydroxymethyl functional group, while the multiple vibrational peaks between 750 and 900 cm^{-1} could be attributed to different methyl substitution patterns in the aromatic ring [39]. Clearly, FT-IR spectra demonstrate that functional groups contribute to molecular scale polarization loss in [Co/NC]@NC-600 [40].

The morphology of ZIF-67, ZIF-67@PR, and [Co/NC]@NC-T samples was characterized by scanning electron microscopy (SEM) as displayed in Fig. 3. In Fig. 3a, it can be observed that the as-obtained ZIF-67 exhibits a dodecahedral shape with an edge size of approximately 500 nm and particle size of around 1 μm. After coating ZIF-67 with phenolic formaldehyde resin, the resulting ZIF-67@PR maintains its dodecahedral morphology while showing a distinct resin layer attached to its surface. Meanwhile, it can be observed that the sample surface exhibits irregular two-dimensional lamellar morphology, which can be attributed to the addition of ammonia that causes the free cobalt ions on the surface of ZIF-67 particles to initially form cobalt hydroxide and subsequently be encapsulated by PR shell. Upon carbonization of ZIF-67@PR, a comparison between Fig. 3c–f reveals that the obtained [Co/NC]@NC-T particles, protected by the PR shell, still maintain a relatively complete rhombic dodecahedral shape and only a small amount

of micropores are generated on the surface due to the collapse of the resin upon carbonization, which is noticeably different from the carbonization of ZIF-67. Furthermore, as the carbonization temperature increases, the shape of [Co/NC]@NC-T does not exhibit significant collapse or shrinkage, with the carbonized phenol-formaldehyde resin maintaining its pre-carbonization morphology. Therefore, it can also be observed that the SEM images of [Co/NC]@NC-T with different pyrolysis temperatures display similar microstructural features.

To estimate the distribution of internal metallic cobalt in [Co/NC]@NC-600, TEM, HRTEM, and energy-dispersive X-ray spectroscopy (EDS) were characterized on the [Co/NC]@NC-600 sample, as shown in Fig. 4. It can be seen that the [Co/NC]@NC-600 particles manifest a distinct hollow architecture with abundant metallic cobalt particles dispersed in the carbon framework (Fig. 4a). Furthermore, in comparison to the [Co/NC]@NC-550 particles displayed in Fig. S6 (Supporting Information), which predominantly consist of around 10-nm metallic cobalt particles, the [Co/NC]@NC-600 particles exhibit a remarkable increase in the size of the metallic cobalt particles which are facilitated by in situ thermal oscillations that break through the carbon encapsulation, resulting in the abnormal growth of crystal grains with particle diameters ranging from 40 to 85 nm. Obviously, the larger metallic particles exhibit a reduced distribution of surface carbon due to the decrease in specific surface area, which, in turn, leads to an abnormally increased I_D/I_G value in the Raman spectrum in Fig. 2b.
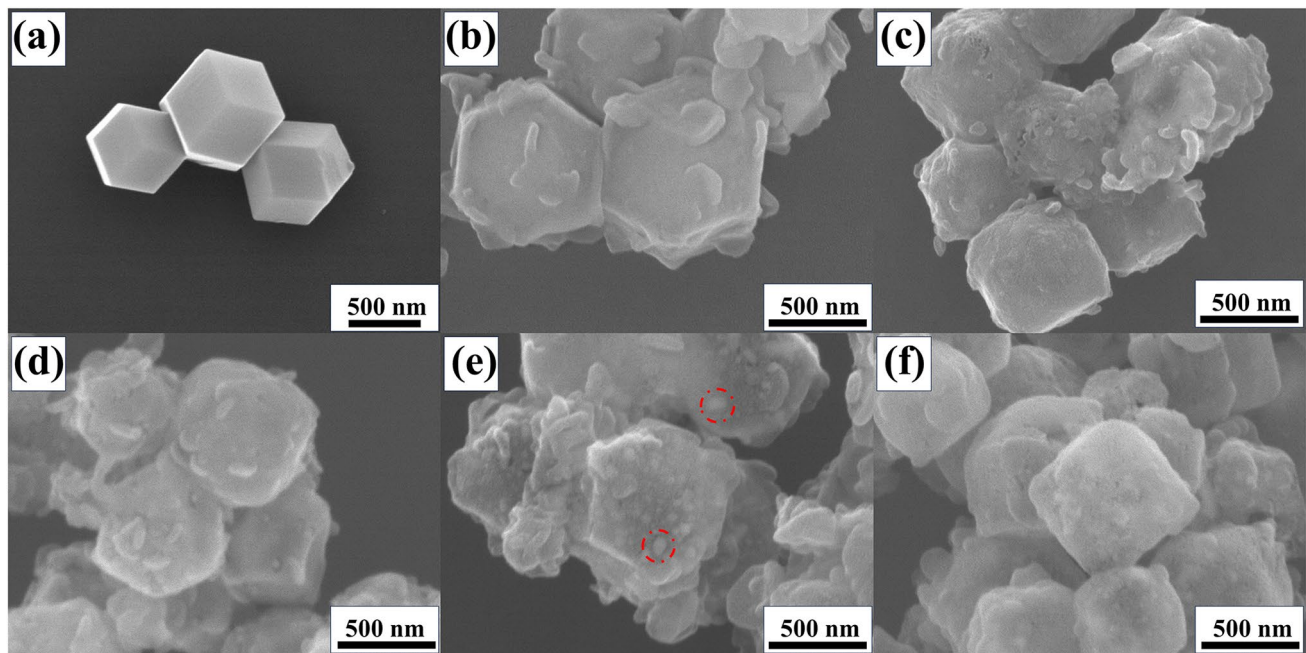

Fig. 3 SEM images of ZIF-67, ZIF-67@RF, and [Co/NC]@NC-T: **a** ZIF-67, **b** ZIF-67@RF, **c** [Co/NC]@NC-500, **d** [Co/NC]@NC-550, **e** [Co/NC]@NC-600, **f** [Co/NC]@NC-650
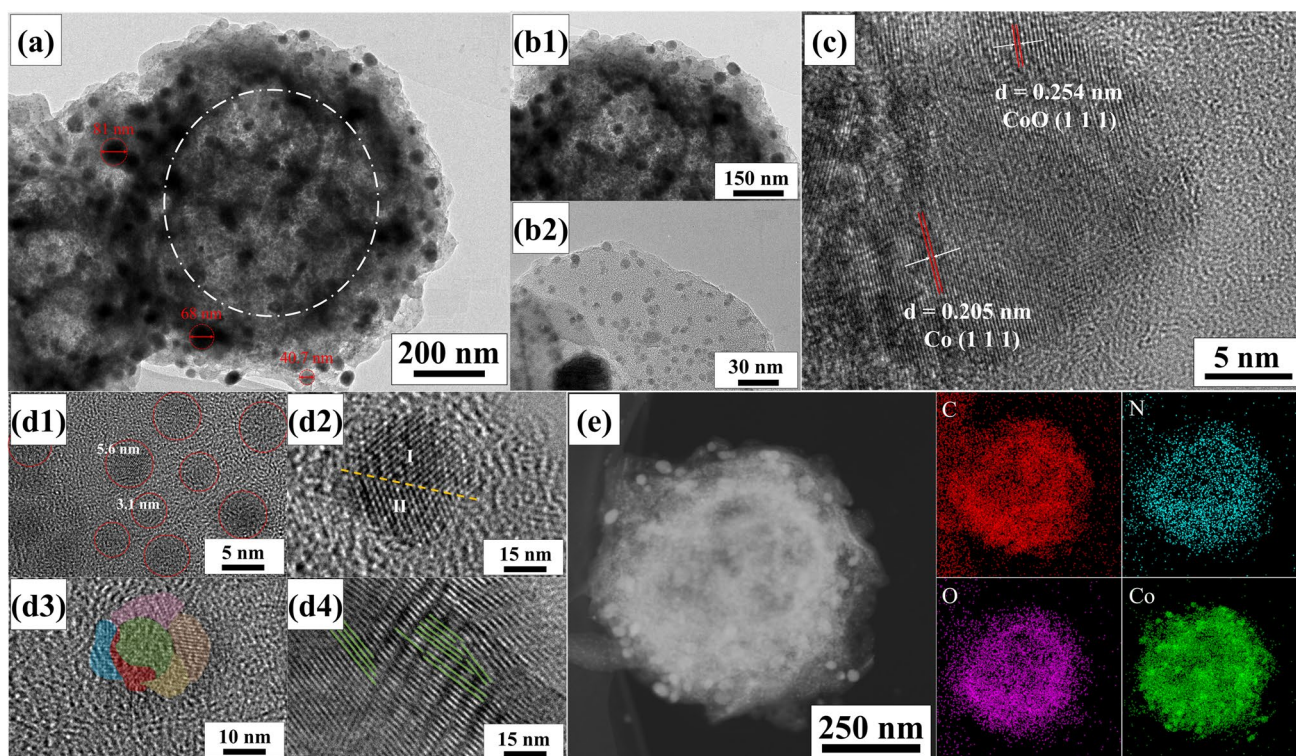
Fig. 4 **a–d** TEM and HRTEM images of [Co/NC]@NC-600; **e** HAADF image and elemental mapping images of [Co/NC]@NC-600

What is more, it is obvious that there are plenty of metallic CQDs with sizes approximately around 5 nm dispersed in the flaky-like carbon as displayed in Fig. 4b1, b2. In the HRTEM image as displayed in Fig. 4c, lattice fringes with a spacing of 0.205 nm can be observed in the quantum dots, which can be attributed to the (111) crystal plane of FFC cobalt. However, there is also a partial oxide layer present outside the quantum dots, with lattice fringe spacing of 0.254 nm index to the (111) crystal plane of CoO. Apparently, there exists a widespread distribution of heterointerfaces between the CQDs, CoO, and amorphous carbon matrix. According to the Maxwell-Wagner-Sillars principle, the differences in Femi level among these products will induce the accumulation of charges at the heterointerfaces, thereby contributing to ideal heterointerface polarization [41, 42]. On the other hand, it can be observed from Fig. 4d that the CQDs obtained through stress-induced nucleation and growth harbor a significant number of lattice defects, such as vacancies, dislocations, and twins. These lattice defect sites act as charge carrier traps, facilitating the formation of atomic-scale dipole moments and consequently leading to corresponding polarization relaxation and EMW attenuation [43, 44].

Furthermore, EDS element mapping images manifest the widespread distribution of C, N, and O elements in [Co/NC]@NC-600 particles as a form of dodecahedral framework (Fig. 4e). Well-founded, the collective distribution of aforementioned elements, combined with XPS spectra, confirms the incorporation of N and O atoms into the carbon matrix as centers for polarization relaxation. Homoplastically, the mapping image of the O element, along with the XPS and FT-IR spectrum, further substantiates the presence of oxygen-containing functional groups within the carbon shell derived from the pyrolysis of the PR shell. Besides, the widespread distribution of Co element in [Co/NC]@NC-600 particles demonstrates the abundant existence of magnetic cobalt particles and cobalt quantum dots within the carbon matrix, indirectly providing evidence for the existence of interface polarization phenomena.

In order to verify the above speculation on the loss mechanism and to characterize the loss performance of EMWs, the electromagnetic parameters in the range of 2–18 GHz of the prepared [Co/NC]@NC-T were characterized as manifested in Fig. 5. In light of Maxwell's equation, the EMW absorption properties of materials are related to the complex dielectric constant (ε_r) and complex permeability (μ_r), in which the real part (ε' and μ') represents the electromagnetic energy storage capacity and the imaginary part (ε'' and μ'') represents the electromagnetic energy attenuation capacity [45]. In addition, the actual dielectric loss capacity and magnetic loss capacity of the materials to the EMWs can be expressed by $\tan\delta_\varepsilon$ ($\varepsilon''/\varepsilon'$) and $\tan\delta_\mu$ (μ''/μ'),
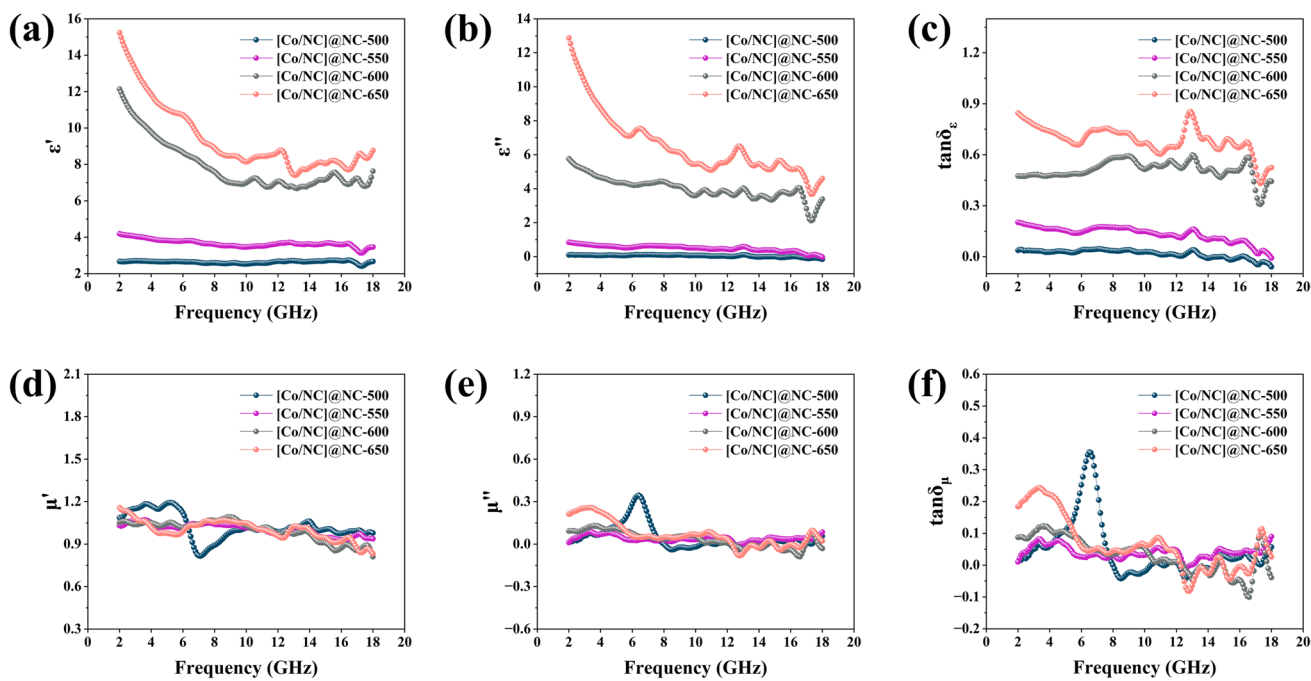
Fig. 5 Electromagnetic parameters of [Co/NC]@NC-T: **a** ε'; **b** ε''; **c** $\tan\delta_\varepsilon$; **d** μ'; **e** μ''; **f** $\tan\delta_\mu$

respectively [46]. It can be seen from Fig. 5a that with the increase of pyrolysis temperature, the ε' of the samples also increases. At the same time, with the increase of frequency, the ε' curves of different samples exhibit a declining tendency, which corresponds to a typical frequency dispersion phenomenon [47]. On the other hand, the ε'' curves of samples in Fig. 5b also increase significantly with the increase of pyrolysis temperature, which is due to the free electron theory [48]:

$$\varepsilon'' = \frac{\sigma}{2\pi\epsilon_0 f} + \frac{(\epsilon_s - \epsilon_\infty)2\pi f\tau}{1 + (2\pi f\tau)^2} \tag{1}$$

where σ presents the conductivity, ε_0 presents the vacuum permittivity, f stands for the frequency, ε_s is the static permittivity, ε_∞ presents the relative permittivity at infinite frequency, and τ stands for the relaxation time. Therefore, with the increase of pyrolysis temperature, the degree of carbonization of the originally non-conductive organic frameworks and PR increases, and the growth of metal cobalt particles increases the degree of graphitization on the surface of the internal cobalt particles, which jointly increases the conductivity of the samples and finally represented by a substantial increase in the ε'' value in the whole frequency range. Moreover, the ε'' curves of different samples show multiple relaxation peaks in the frequency band higher than 5 GHz, which may represent a large amount of polarization loss in MAMs. With the increase of pyrolysis temperature, the same trend as the ε'' curves is also displayed on the $\tan\delta_\varepsilon$ curves,

which indicates that the dielectric loss capacity of the samples increases with the increase of pyrolysis temperature.

Figure 5d–f display μ', μ'', and $\tan\delta_\mu$ curves of each sample in the frequency range of 2–18 GHz, respectively. Obviously, the μ' and μ'' of different samples have close values in the frequency band above 8 GHz, and this value is very close to the air, representing that the sample has basically no magnetic loss capability in this frequency range. Combined with TEM image analysis, this phenomenon may be attributed to the fact that as single-domain particles, the magnetization and demagnetization of CQDs involve rotational processes of the magnetization vector, leading to a decrease in permeability. Hence, what contributes to the magnetic loss in the samples should be the natural resonance of the magnetic nanoparticles, corresponding to the peak of the μ'' curves in the frequency band of 2–8 GHz. It is noteworthy that the μ' and μ'' curves of [Co/NC]@NC-500 exhibit a typical Lorentz model of natural resonance around 6 GHz, which may be due to the small size of magnetic cobalt particles generated by low pyrolysis temperature and fewer defects in the crystals, thus reducing the damping factor α and leading to an increase in the natural resonance frequency [49, 50]. In addition, the $\tan\delta_\mu$ values of other samples except [Co/NC]@NC-500 are significantly smaller than $\tan\delta_\varepsilon$, which indicates that the dielectric loss mechanism is dominant in these samples.

For magnetic loss MAMs, effective attenuation mechanisms in the GHz band include natural resonance, eddy

current resonance, and exchange resonance [51, 52]. In order to explore the influence of different magnetic loss mechanisms in different frequency bands, the following formula is introduced [17]:

$$C_0 = \mu''\left(\mu'\right)^{-2} f^{-1} \tag{2}$$

According to the formula, C_0 is a frequency-dependent quantity. When the value of C_0 remains constant, eddy current loss is the only magnetic loss mechanism in the current frequency band. Figure 6a shows the frequency variation of C_0 values of different samples in the range of 2–18 GHz. It is evident that within the frequency range of 2–10 GHz, the C_0 values of the various samples exhibit variability alongside noticeable vibration peaks, which suggests that the primary magnetic loss mechanism occurring in the samples within this frequency band is attributed to natural resonance. In the 10–18 GHz band, the C_0 curves of different samples all manifest frequent and weak vibration peaks, which is due to the similar size exchange resonance caused by the uneven size of the metallic cobalt particles inside the particles.

Based on the transmission line theory, the attenuation constant α represents the ability to attenuate EMWs for MAMs, which can be defined as [53]:

$$\alpha = \frac{\sqrt{2}\pi f}{c} \sqrt{\left(\mu''\epsilon'' - \mu'\epsilon'\right) + \sqrt{\left(\mu''\epsilon'' - \mu'\epsilon'\right)^2 + \left(\mu'\epsilon'' + \mu''\epsilon'\right)^2}} \tag{3}$$

where c is the velocity of EMWs in a vacuum. As can be seen from Fig. 6b, [Co/NC]@NC-650 and [Co/NC]@NC-600 exhibit excellent attenuation performance to EMWs in the whole frequency band, reaching peaks of 572 and 398 at 16.3 GHz, respectively. This excellent attenuation ability corresponds to the excellent ϵ'' and μ'', and the four samples show a positive correlation with the carbonization temperature. In addition, [Co/NC]@NC-500 exhibits better microwave attenuation performance than [Co/NC]@NC-550 near 6.3 GHz, due to its better magnetic loss capacity in this band.

At the same time, to further validate the previous description of multi-scale loss mechanism coupling in the synthesized [Co/NC]@NC-T, Cole-Cole semicircle was used to characterize the polarization loss, which can be derived from Debye dipole relaxation formula (4):

$$\left(\epsilon' - \frac{\epsilon_s + \epsilon_\infty}{2}\right)^2 + \left(\epsilon''\right)^2 = \left(\frac{\epsilon_s - \epsilon_\infty}{2}\right)^2 \tag{4}$$

According to the Cole-Cole semicircle formula, when MAMs undergo dielectric relaxation, the curve composed of ϵ' and ϵ'' should represent a semicircle. In order to further confirm the contribution of Debye dipole relaxation to the dielectric loss properties of samples, Cole-Cole semicircle curves of different samples are shown in Fig. 6c–f. It can be found that obvious Cole-Cole semicircles appear in the curves of samples with different pyrolysis temperatures,
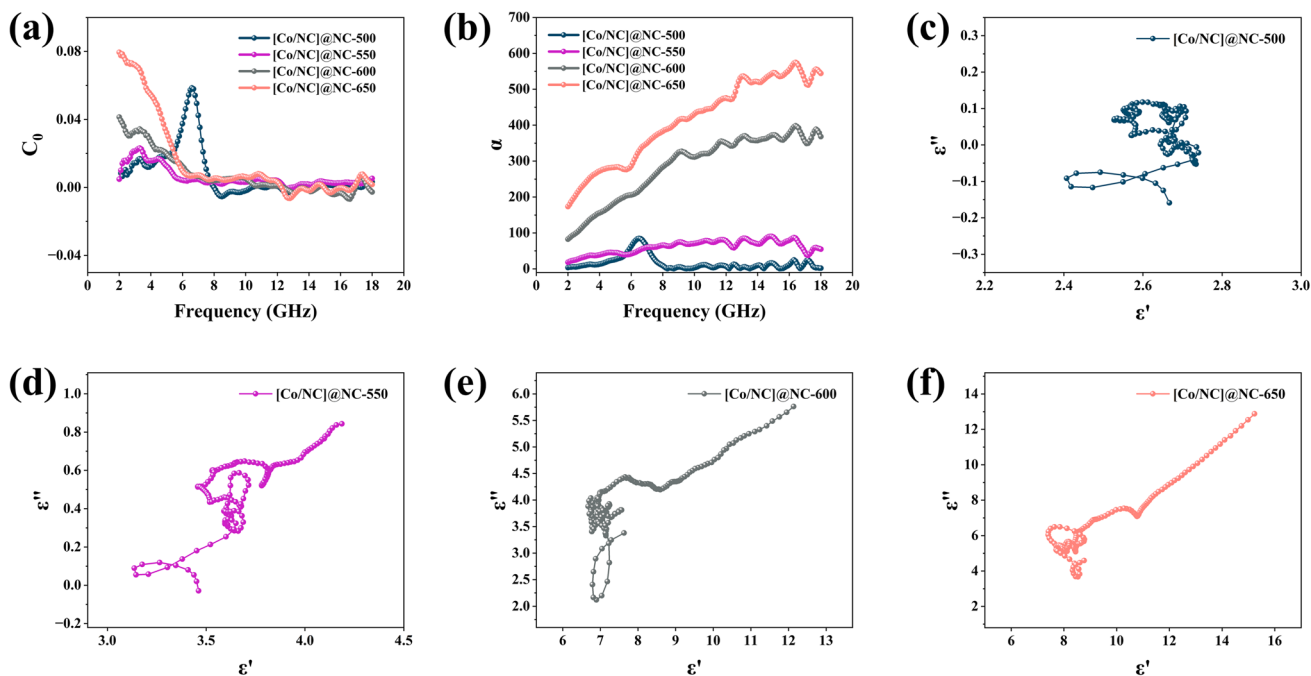

Fig. 6 **a** C_0 curves of [Co/NC]@NC-T; **b** the attenuation constants α of [Co/NC]@NC-T; **c–f** Cole-Cole semicircles of [Co/NC]@NC-T

and there are many different semicircles, which represents the existence of multiple dielectric polarization relaxation phenomena. In addition, except for [Co/NC]@NC-500, the Cole-Cole curves of other samples have straight lines at the end, which represents the dominant conductance loss at the low-frequency band [54]. Meanwhile, with the increase of pyrolysis temperature, it is obvious that the proportion of linear parts also increases significantly, which is owing to the increase of pyrolysis temperature promoting the decomposition of non-conductive organic frameworks and PR.

Based on the complex permittivity and complex permeability of MAMs, the reflection loss (RL) can be calculated by the transmission line theory as follows [53, 55]:

$$RL\,(dB) = 20log\left|\frac{Z_{in} - Z_0}{Z_{in} + Z_0}\right| \tag{5}$$

where Z_0 represents the free space impedance and Z_{in} stands for the input impedance of the material, and the calculation formula is as follows:

$$Z_{in} = Z_0\sqrt{\frac{\mu_r}{\epsilon_r}}tanh\left[j\left(\frac{2\pi}{c}\right)fd\sqrt{\mu_r\epsilon_r}\right] \tag{6}$$

in which c represents the speed of light in free space and d represents the thickness of the absorber. Figure 7 exhibits the RL value curve of [Co/NC]@NC-T in the frequency range of 2–18 GHz and d in the thickness range of 1–5 mm. As can be seen from the RL curves and 3D RL diagrams of [Co/NC]@NC-500 and [Co/NC]@NC-550 in Fig. 7a–f, the samples have no effective microwave absorption performance in the full frequency band, which is mainly due to the low electrical conductivity caused by low pyrolysis temperature. Subsequently, with the increase of pyrolysis temperature, the dielectric properties of the samples are significantly improved. What is more, the abnormal growth of metallic cobalt particles also increases the size distribution from the range of 3–15 nm to 3–85 nm, which provides more types of magnetic losses. Under the double increase of dielectric loss and magnetic loss, as shown in Fig. 7g–i, the RL_min value of [Co/NC]@NC-600 reaches − 57.0 dB at 17.9 GHz when the thickness is 1.73 mm, and the EABD reaches the

maximum value of 5.7 GHz when the thickness is 2 mm. When the carbonization temperature reaches 650 °C, further carbonization of the organic occurs in [Co/NC]@NC-650, resulting in an improved dielectric loss capacity. Nevertheless, the increase in magnetic loss is minimal, which leads to an imbalance in impedance matching, thereby restricting the acquisition of more ideal EMW absorption performance. Hence, the [Co/NC]@NC-650 exhibits a puny microwave absorption performance with RL_min value at 17.3 GHz at 1.63 mm thickness is −16.5 dB, and the EABD reaches a maximum of 4.7 GHz at a thickness of 1.77 mm (Fig. 7j–l). The reflection loss properties of some typical Co and Co/C composites that have been published and cited most in recent years are listed in Table 1 for comparison. It can be found that the EMW absorption performance of [Co/NC]@NC-600 prepared in this work is comparable to or even better than most materials due to the unique multi-scale loss mechanism coupling effect of precise design, which verifies the reliability of this work, and also indicates that [Co/NC]@NC-600 is an ideal candidate for an efficient EMW absorber [56–61].

In order to further prove the EMW absorption characteristics of [Co/NC]@NC-T sample under practical application conditions, RCS simulation was carried out by CST studio. The constructed simulation model consists of an absorber layer and a perfect electric conductor (PEC) layer, as shown in Fig. S7 (Supporting Information). The reflected signal intensity of the four models is simulated under the vertical incident EMW. The 3D RCS distribution of [Co/NC]@NC-T shows similar scattering signals of 3D radar waves (Fig. 8a–d), where [Co/NC]@NC-500 and [Co/NC]@NC-550 have basically no absorption capacity, while [Co/NC]@NC-600 has the least vertical reflection intensity. The results show that [Co/NC]@NC-600 has a strong attenuation ability of incident microwave, which is consistent with the RL calculation results.

According to the above discussion, the multi-scale loss mechanism of the prepared [Co/NC]@NC-600 is summarized in Fig. 8f. (1) In the atomic-scale loss mechanism, a large number of N and O atoms that existed in the ZIF-67 will be doped into the carbon matrix after pyrolysis. These

Table 1 Comparison of [Co/NC]@NC-600 composites with other Co/C composites

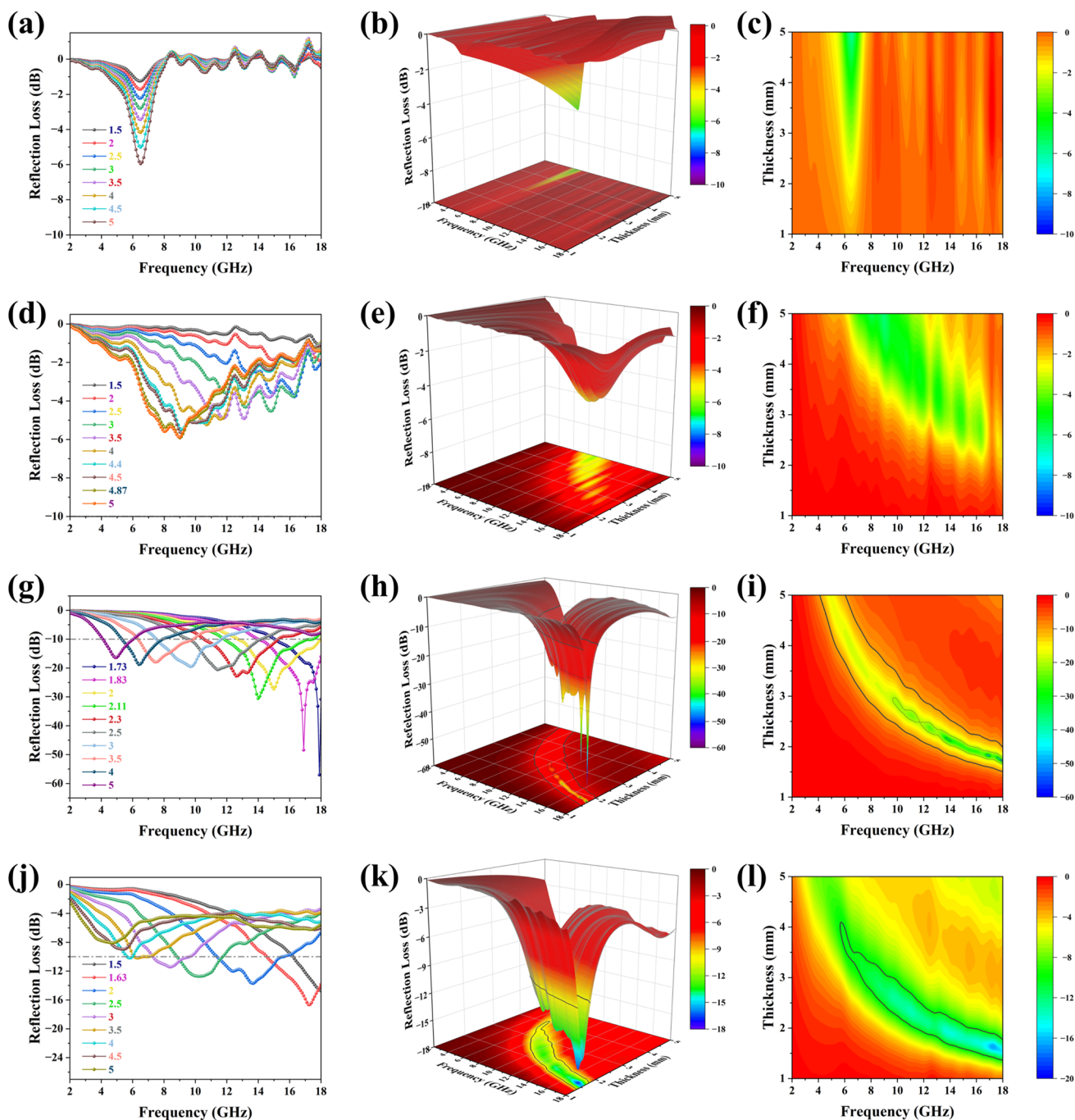| Samples	Reflection loss (dB)	Corresponding thickness (mm)	EAB (GHz)	Corresponding thickness (mm)	Reference
Co/C-800	−32.4	2.0	3.8	2.0	[56]
Z67-8@C	−58.1	2.5	5.7	2.0	[57]
CoNi@GC/BN-HCPs	−62.8	3.0	8	2.0	[58]
Co@NCNS-800	−60.6	2.4	5.1	1.9	[59]
YS-Co/C-700	−57.34	2.5	5.6	2.5	[60]
In/C@Co/C-800	−55.14	2.19	5.68	2.13	[61]
[Co/NC]@NC-600	−57.0	1.73	5.7	2.0	★ This work

Fig. 7 RL curves of [Co/NC]@NC-T: **a–c** [Co/NC]@NC-500; **d–f** [Co/NC]@NC-550; **g–i** [Co/NC]@NC-600; **j–l** [Co/NC]@NC-650

atoms, along with the defects in the carbon matrix stemming from the pyrolysis process, contribute to the dielectric loss capacity by acting as dipole moments at the atomic scale. In addition, numerous lattice defects such as vacancies, dislocations, and twin boundaries in the grown cobalt quantum dots will also provide polarization loss as the polarization sites trap free carriers [62]. (2) In the molecular scale loss mechanism, plenty of functional groups such as the phenolic

hydroxyl group in the PR shell can be preserved by reasonable control of pyrolysis, thus providing a molecular dipole loss mechanism. (3) In the crystal scale loss mechanism, the first is the magnetic loss capacity contributed by magnetic nanoparticles. In order to explore the magnetic properties of magnetic particles of different scales, the array composed of these particles was simulated by micromagnetic theory. The results are shown in Fig. 8e, and further details can be found
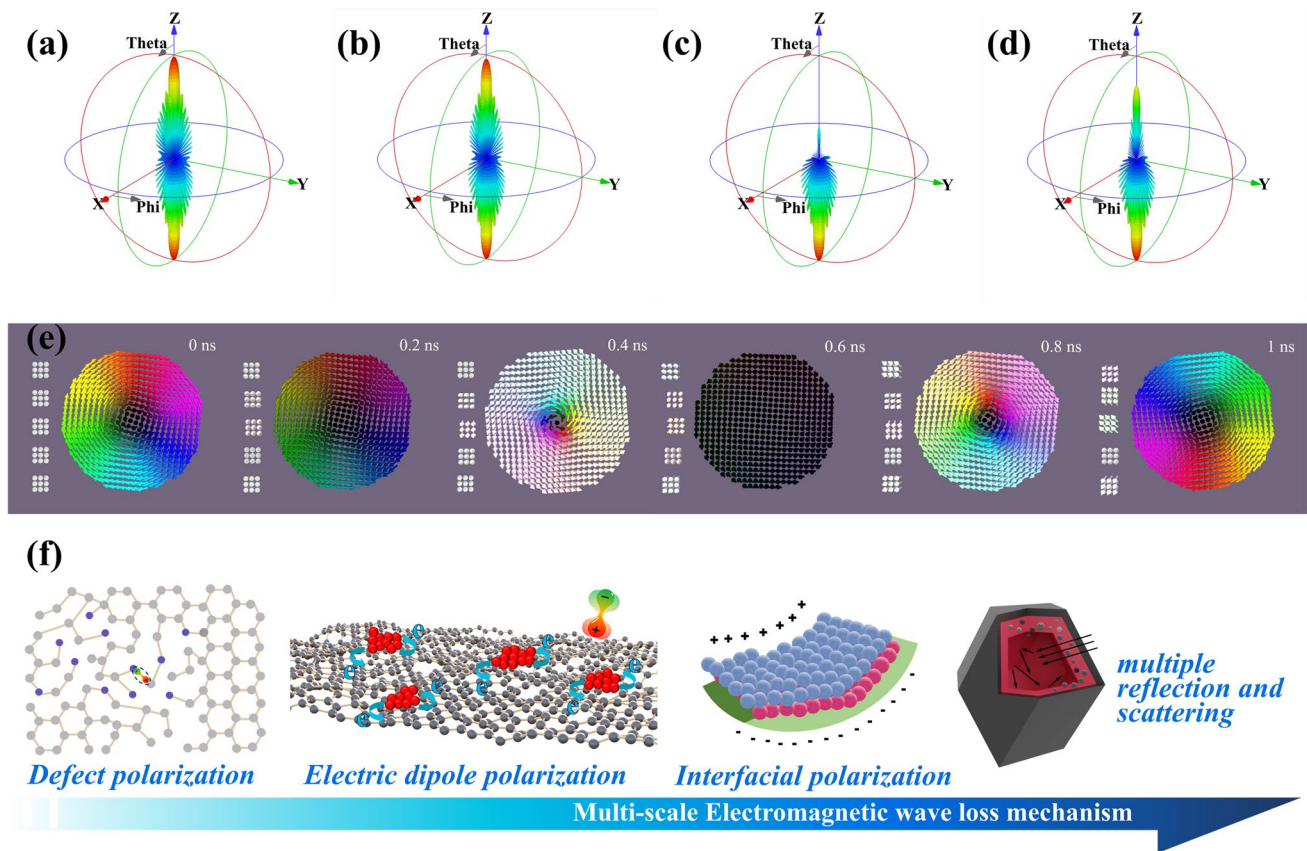
Fig. 8 CST Simulation results of **a** [Co/NC]@NC-500, **b** [Co/NC]@NC-550, **c** [Co/NC]@NC-600, and **d** [Co/NC]@NC-650; **e** the micromagnetic simulation of the magnetic array; **f** schematic illustration of the multi-scale electromagnetic wave loss mechanism

in the Supporting Information. It is clear that CQDs with a diameter of 5 nm behave as typical single-domain particles with magnetic domains that hardly respond to alternating magnetic fields. Correspondingly, magnetic particles with a diameter of 50 nm exhibit typical vortex domain states, and the rotation of the vortex changes with the alternating magnetic field. In this process, the induced magnetic field changes gradually lag behind the alternating magnetic field, thus contributing to the magnetic loss capacity [63, 64]. In addition, other mechanisms such as natural resonance, exchange resonance, and eddy current loss also contribute to the magnetic loss capacity. In terms of dielectric loss, due to the difference in conductivity, a large amount of charge accumulates at the interface between metallic cobalt, CoO, and carbon matrix, causing the phenomenon of heterogeneous interface polarization [65–67]. (4) In the mesoscopic-scale loss mechanism, the hollow structure of prepared [Co/NC]@NC-600 also contributes to the absorption of EMW. This hollow structure not only reduces the density, but also expands the transmission path of EMW in the absorber by providing multiple reflection and scattering of EMW. Moreover, based on the Maxwell Garnett theory, the introduction of air into the absorber optimizes the overall impedance

matching characteristics of the absorber, promoting the EMW incident into the absorber and eventually being lost [68–70]. There is no doubt that the excellent EMW absorption ability of the prepared [Co/NC]@NC-600 with wide EABD and high RL value is achieved through the coupling of these multi-scale loss mechanisms.

3 Conclusions

In general, we successfully prepared N-doped Co/C composites with hollow structures by wet chemistry and pyrolysis treatment process. Due to the precise synthetic technique, the prepared [Co/NC]@NC-T electromagnetic wave absorption material achieves the retention of numerous functional groups while featuring a range of magnetic particles of various sizes. Additionally, it also exhibits significant doping of impurity atoms and abundant heterogeneous interface polarization. When the pyrolysis temperature is 600 °C, the obtained [Co/NC]@NC-600 simultaneously realizes the coupling of the above multi-scale loss mechanism, and obtains outstanding electromagnetic wave absorption performance: the RL_{min} value reaches −57.0 dB at 17.9 GHz

when the thickness is 1.73 mm, and the EABD reaches the maximum value of 5.7 GHz when the thickness is 2 mm. This work is a simple way to realize the wideband MAMs with a multi-scale coupling loss mechanism, which provides a reliable template for the subsequent design of electromagnetic wave absorption materials.

4 Experimental section

4.1 Chemicals

Cobalt nitrate hexahydrate $(Co(NO_3)_2 \cdot 6H_2O)$, $NH_3 \cdot H_2O$, carbinol, and ethanol were purchased from Shanghai Sinopharm Chemical reagent Co. Ltd. 2-Methylimidazole (2-MeIm) and formaldehyde solution were purchased from Shanghai Aladdin Biochemical Technology Co. Ltd. Resorcinol were purchased from Alfa Aesar (China) Chemicals Co. Ltd. Deionized water used in all experiments was obtained from a Milli-Q system (Millipore, Bedford, MA, USA). All chemicals used in the experiments were of analytical grade without further purification.

4.2 Preparation of ZIF-67 precursors

The synthesis of ZIF-67 precursors was performed using a similar method reported in the literature [71]. Namely, 8 mmol $Co(NO_3)_2 \cdot 6H_2O$ and 32 mmol 2-methylimidazole (2-MeIm) were both dissolved in 200-mL carbinol, and then, the latter was rapidly poured into the former under vigorous stirring, for which a homogeneous purple solution was obtained after continuously stirring for 30 min. The resultant suspension, after being aged for 24 h, was collected by suction filtration, purified using ethyl alcohol (EtOH), and dried at 60 °C for 24 h.

4.3 Preparation of ZIF-67@PR precursors

The coating of the PR shell was also performed as reported before [72]. Briefly, place 100 mg ZIF-67, acquired in Step 2.2, into a 200-mL beaker. Add 32 mL of ethanol and subject it to 20 min of ultrasonic dispersion. Subsequently, add 400 μL of $NH_3 \cdot H_2O$ solution and 80 mL of deionized water to the beaker, and then place it on a magnetic stirrer for agitation. Sequentially incorporate 200 mg of resorcinol. Once the resorcinol is entirely dissolved, add 280 μL of formaldehyde solution. Allow the mixture to stir at room temperature for 12 h. As a final step, utilize centrifugation at 4500 rpm for 5 min to isolate the ZIF-67@PR product, and then proceed with six alternating deionized water and ethanol washes. Lastly, dry at 60 °C for 24 h.

4.4 Preparation of [Co/NC]@NC-T

Finally, the obtained ZIF-67@PR were carbonized accompanied by an Ar atmosphere for 2 h with a heating rate at 2 °C/min in the tubular furnace, respectively. The black powder acquired was named [Co/NC]@NC-T (*T* refers to the carbonization temperature, *T* = 500, 550, 600, 650).

4.5 Characterization

The crystalline structures and phase composition of obtained products were characterized by X-ray diffraction (XRD, smartlab 9) with a Cu Kα source (40 KV, 200 mA). Scanning electron microscopy (SEM, JSM-7001 F) with an accelerating voltage of 20 kV and transmission electron microscopy (TEM, JEM-2100 F) with an accelerating voltage of 200 kV were used to characterize the morphology and size of samples. The X-ray photoelectron spectrometer (XPS, Axis Supra) was measured on an Axis Supra with an Al Kα X-ray source. The Raman spectra were measured by Raman spectrometer (Xplora plus, HOBIRA) and FT-IR spectra were measured on a Fourier transform infrared spectrometer (Thermo Fisher Scientific, iS5-iD1) in the region of 4000–500 cm^{-1}. The nitrogen adsorption-desorption isotherms were collected using a Micromeritics ASAP 2020 M surface area analyzer at 77 K. The content of the carbon matrix was characterized by the diamond TGA/DTA analyzer (SETSYS18TG/DTA/DSC). The relative complex permeability and relative permittivity of the sample in the frequency range of ability and relative permittivity of the sample in the frequency range of 2–18 GHz were characterized by a vector network analyzer (VNA, Agilent N5234A). After mixing the products with the paraffin in the mass ratio of 3:7 uniformly, the annular sample with outer diameter of 7 mm and inner diameter of 3 mm was pressed, and the thickness was about 3.00 mm. The subsequent research on mixing our products with epoxy for the future practical test of electromagnetic performance will be conducted as well.

4.6 Radar cross-section (RCS) simulation

The RCS values were simulated using CST Studio Suite 2022. The simulation model was a square (180 mm of side length), comprising a top absorber (thickness = 1.73 mm) and a bottom perfect electric conductor (1 mm of side length). The simulation was set on the XOY plane to describe the RCS, and the EM wave propagated along the negative direction of the Z-axis, while the electric polarization direction of the EM wave was designed to propagate

along the X-axis. Open boundary conditions were set in all directions, while the scattering direction was dependent on theta and phi in polar coordinates. Calculations were performed by means of a time domain solver, which enabled the determination of the monostatic RCS. The RCS can be described as follows:

$$\sigma\left(dBm^2\right) = 10log\left(\frac{4\pi S}{\lambda^2}\left|\frac{E_s}{E_i}\right|^2\right) \tag{7}$$

where λ is the wavelength, S is the area, E_i represents the electric field intensity of the receiving waves, and E_s is the electric field intensity of the transmitting waves.

Data availability No datasets were generated or analysed during the current study.

Declarations

Competing interests The authors declare no competing interests.

References

1. Li B, Wang F, Wang K et al (2022) Metal sulfides based composites as promising efficient microwave absorption materials: a review. J Mater Sci Technol 104:244–268. https://doi.org/10.1016/j.jmst.2021.06.065
2. He P, Zheng M-J, Liu Q et al (2022) MXene nanohybrids: excellent electromagnetic properties for absorbing electromagnetic waves. Ceram Int 48:1484–1493. https://doi.org/10.1016/j.ceramint.2021.10.049
3. Liang L, Yu R, Ong SJH et al (2023) An adaptive multispectral mechano-optical system for multipurpose applications. ACS Nano 17:12409–12421. https://doi.org/10.1021/acsnano.3c01836
4. Liu Y, Wang Y, Wu N et al (2023) Diverse structural design strategies of MXene-based macrostructure for high-performance electromagnetic interference shielding. Nanomicro Lett 15:240. https://doi.org/10.1007/s40820-023-01203-5
5. Idris FM, Hashim M, Abbas Z et al (2016) Recent developments of smart electromagnetic absorbers based polymer-composites at gigahertz frequencies. J Magn Magn Mater 405:197–208. https://doi.org/10.1016/j.jmmm.2015.12.070
6. Lv H, Yang Z, Pan H et al (2022) Electromagnetic absorption materials: current progress and new frontiers. Prog Mater Sci. https://doi.org/10.1016/j.pmatsci.2022.100946
7. Cheng J, Zhang H, Ning M et al (2022) Emerging materials and designs for low- and multi-band electromagnetic wave absorbers: the search for dielectric and magnetic synergy? Adv Funct Mater. https://doi.org/10.1002/adfm.202200123
8. Xu H, Zhang G, Wang Y et al (2022) Size-dependent oxidation-induced phase engineering for MOFs derivatives via spatial confinement strategy toward enhanced microwave absorption. Nano-Micro Lett. https://doi.org/10.1007/s40820-022-00841-5
9. Ren Y, Wang X, Ma J et al (2023) Metal-organic framework–derived carbon–based composites for electromagnetic wave absorption: dimension design and morphology regulation. J Mater Sci Technol 132:223–251. https://doi.org/10.1016/j.jmst.2022.06.013
10. Yang H, Shen Z, Peng H et al (2021) 1D–3D mixed-dimensional MnO_2@nanoporous carbon composites derived from Mn-metal organic framework with full-band ultra-strong microwave absorption response. Chem Eng J. https://doi.org/10.1016/j.cej.2020.128087
11. Liu W, Tan S, Yang Z et al (2018) Hollow graphite spheres embedded in porous amorphous carbon matrices as lightweight and low-frequency microwave absorbing material through modulating dielectric loss. Carbon 138:143–153. https://doi.org/10.1016/j.carbon.2018.06.009
12. Rodenas T, Luz I, Prieto G et al (2014) Metal-organic framework nanosheets in polymer composite materials for gas separation. Nat Mater 14:48–55. https://doi.org/10.1038/nmat4113
13. Sun H, Che R, You X et al (2014) Cross-stacking aligned carbon-nanotube films to tune microwave absorption frequencies and increase absorption intensities. Adv Mater 26:8120–8125. https://doi.org/10.1002/adma.201403735
14. Ai K, Liu Y, Ruan C et al (2013) Sp^2C-dominant N-doped carbon sub-micrometer spheres with a tunable size: a versatile platform for highly efficient oxygen-reduction catalysts. Adv Mater 25:998–1003. https://doi.org/10.1002/adma.201203923
15. Li B, Ma Z, Zhang X et al (2023) NiO/Ni heterojunction on N-doped hollow carbon sphere with balanced dielectric loss for efficient microwave absorption. Small. https://doi.org/10.1002/smll.202207197
16. Xiao L, Cheng C, Li Z et al (2023) Dynamically modulated synthesis of hollow metal-organic frameworks for selective hydrogenation reactions. Nano Res 16:11334–11341. https://doi.org/10.1007/s12274-023-5750-7
17. Chen C, Shan Z, Tao S et al (2023) Atomic tuning in electrically conducting bimetallic organic frameworks for controllable electromagnetic wave absorption. Adv Funct Mater. https://doi.org/10.1002/adfm.202305082
18. Yin P, Yao T, Wu Y et al (2016) Single cobalt atoms with precise N-coordination as superior oxygen reduction reaction catalysts. Angew Chem Int Ed 55:10800–10805. https://doi.org/10.1002/anie.201604802
19. Zhang Q, Wang H, Han W et al (2022) Core-shell prussian blue analogues derived from metal-organic frameworks as efficient electrocatalysts for oxygen evolution reaction. Nano Res 16:3695–3702. https://doi.org/10.1007/s12274-022-4832-2
20. Chi Z, Feng Y, Ma Y et al (2021) Polydopamine-coated bimetallic ZIF derivatives as an air cathode for acidic Zn-air batteries with super-high potential. Chem Commun 57:11248–11251. https://doi.org/10.1039/d1cc04443e

21. Gao Z, Iqbal A, Hassan T, Zhang L, Wu H, Koo CM et al (2022) Texture regulation of metal-organic frameworks, microwave absorption mechanism-oriented structural optimization and design perspectives. Adv Sci 9(35):2204151. https://doi.org/10.1002/advs.202204151

22. Gao T, Zhao R, Li Y et al (2022) Sub-nanometer Fe clusters confined in carbon nanocages for boosting dielectric polarization and broadband electromagnetic wave absorption. Adv Funct Mater. https://doi.org/10.1002/adfm.202204370

23. Wang Y-L, Yang S-H, Wang H-Y et al (2020) Hollow porous CoNi/C composite nanomaterials derived from MOFs for efficient and lightweight electromagnetic wave absorber. Carbon 167:485–494. https://doi.org/10.1016/j.carbon.2020.06.014

24. Huang M, Wang L, You W et al (2021) Single zinc atoms anchored on MOF-derived N-doped carbon shell cooperated with magnetic core as an ultrawideband microwave absorber. Small. https://doi.org/10.1002/smll.202101416

25. Gao Z, Lan D, Zhang L et al (2021) Simultaneous manipulation of Interfacial and defects polarization toward Zn/Co phase and ion hybrids for electromagnetic wave absorption. Adv Funct Mater. https://doi.org/10.1002/adfm.202106677

26. Seifert W, Carlsson N, Miller M et al (1996) In-situ growth of quantum dot structures by the Stranski-Krastanow growth mode. Prog Cryst Growth Charact Mater 33:423–471

27. Johansson J, Seifert W (2002) Kinetics of self-assembled island formation: part I-Island density. J Cryst Growth 234:132–138

28. Osipov A, Kukushkin S, Schmitt F et al (2001) Kinetic model of coherent island formation in the case of self-limiting growth. Phys Rev B 64:205421

29. Banerjee R, Phan A, Wang B et al (2008) High-throughput synthesis of Zeolitic Imidazolate Frameworks and application to CO_2 capture. Science 319:939–943

30. Li Y, Liu R, Pang X et al (2018) Fe@C nanocapsules with substitutional sulfur heteroatoms in graphitic shells for improving microwave absorption at gigahertz frequencies. Carbon 126:372–381. https://doi.org/10.1016/j.carbon.2017.10.040

31. Ma L, Li S, Liu F et al (2022) Metal-organic framework-derived Co/C composite with high magnetization as broadband electromagnetic wave absorber. J Alloys Compd. https://doi.org/10.1016/j.jallcom.2022.164257

32. Li S, Ma L, Lei Z et al (2022) Bifunctional two-dimensional nanocomposite for electromagnetic wave absorption and comprehensive anti-corrosion. Carbon 186:520–529. https://doi.org/10.1016/j.carbon.2021.10.055

33. Liao Q, He M, Zhou Y et al (2018) Highly cuboid-shaped Heterobimetallic metal-organic frameworks derived from porous Co/ZnO/C microrods with Improved electromagnetic wave absorption capabilities. ACS Appl Mater Interfaces 10:29136–29144. https://doi.org/10.1021/acsami.8b09093

34. Liu H, Xu Y, Yong H et al (2023) Studies on electromagnetic interference shielding effect mechanisms of leaf-like three-dimensional carbon nanotubes/graphene aerogel film and the composites with polydimethylsiloxane. Carbon 207:261–269. https://doi.org/10.1016/j.carbon.2023.03.006

35. Liang H, Chen G, Liu D et al (2022) Exploring the Ni 3d Orbital unpaired electrons Induced polarization loss based on Ni single-atoms model Absorber. Adv Funct Mater. https://doi.org/10.1002/adfm.202212604

36. Hou C, Yang W, Kimura H et al (2023) Boosted lithium storage performance by local build-in electric field derived by oxygen vacancies in 3D holey N-doped carbon structure decorated with molybdenum dioxide. J Mater Sci Technol 142:185–195. https://doi.org/10.1016/j.jmst.2022.10.007

37. Yang W, Peng D, Kimura H et al (2022) Honeycomb-like nitrogen-doped porous carbon decorated with Co_3O_4 nanoparticles for superior electrochemical performance pseudo-capacitive lithium storage and supercapacitors. Adv Compos Hybrid Mater 5:3146–3157. https://doi.org/10.1007/s42114-022-00556-6

38. Song X, Mo J, Fang Y et al (2022) Synthesis of magnetic nanocomposite Fe_3O_4@ZIF-8@ZIF-67 and removal of tetracycline in water. Environ Sci Pollut Res 29:35204–35216. https://doi.org/10.1007/s11356-021-18042-9

39. Costa L, Di Montelera LR, Camino G et al (1997) Structure-charring relationship in phenol-formaldehyde type resins. Polym Degrad Stab 56:23–35

40. Zhao Z, Zhang L, Wu H (2022) Hydro/organo/ionogels: controllable electromagnetic wave absorbers. Adv Mater. https://doi.org/10.1002/adma.202205376

41. Yousefi N, Sun X, Lin X et al (2014) Highly aligned graphene/polymer nanocomposites with excellent dielectric properties for high-performance electromagnetic interference shielding. Adv Mater 26:5480–5487. https://doi.org/10.1002/adma.201305293

42. Prodromakis T, Papavassiliou C (2009) Engineering the Maxwell-Wagner polarization effect. Appl Surf Sci 255:6989–6994. https://doi.org/10.1016/j.apsusc.2009.03.030

43. Qin M, Zhang L, Wu H (2022) Dielectric loss mechanism in electromagnetic wave absorbing materials. Adv Sci. https://doi.org/10.1002/advs.202105553

44. Liu Y, Zhou X, Jia Z et al (2022) Oxygen vacancy-induced dielectric polarization prevails in the electromagnetic wave-absorbing mechanism for Mn-based MOFs-derived composites. Adv Funct Mater. https://doi.org/10.1002/adfm.202204499

45. Li D, Jia D, Yang Z et al (2021) Principles, design, structure and properties of ceramics for microwave absorption or transmission at high-temperatures. Int Mater Rev 67:266–297. https://doi.org/10.1080/09506608.2021.1941716

46. Bhattacharjee Y, Bose S (2021) Core-shell nanomaterials for microwave absorption and electromagnetic interference shielding: a review. ACS Appl Nano Mater 4:949–972. https://doi.org/10.1021/acsanm.1c00278

47. Du Y, Liu W, Qiang R et al (2014) Shell thickness-dependent microwave absorption of core–Shell Fe_3O_4@C composites. ACS Appl Mater Interfaces 6:12997–13006. https://doi.org/10.1021/am502910d

48. Wang H, Zhang H, Zhao K et al (2023) Research progress on electromagnetic wave absorption based on magnetic metal oxides and their composites. Adv Compos Hybrid Mater. https://doi.org/10.1007/s42114-023-00694-5

49. Qin F, Peng M, Estevez D et al (2022) Electromagnetic composites: from effective medium theories to metamaterials. J Appl Phys. https://doi.org/10.1063/5.0099072

50. Tsutaoka T (2003) Frequency dispersion of complex permeability in Mn-Zn and Ni-Zn spinel ferrites and their composite materials. J Appl Phys 93:2789–2796. https://doi.org/10.1063/1.1542651

51. Ma B, Chen F, Cheng Y et al (2023) $Ti_3C_2T_x$ MXene@NiFe layered double hydroxide derived multiple interfacial composites with efficient microwave absorption. J Alloys Compd. https://doi.org/10.1016/j.jallcom.2022.168162

52. Wang B, Wu Q, Fu Y et al (2021) A review on carbon/magnetic metal composites for microwave absorption. J Mater Sci Technol 86:91–109. https://doi.org/10.1016/j.jmst.2020.12.078

53. Zhang M, Wang L, Bao S et al (2023) A finite oxidation strategy for customizing heterogeneous interfaces to enhance magnetic loss ability and microwave absorption of Fe-cored carbon microcapsules. Nano Res 16:11084–11095. https://doi.org/10.1007/s12274-023-5511-7

54. Wen C, Li X, Zhang R et al (2021) High-density anisotropy magnetism enhanced microwave absorption performance in $Ti_3C_2T_x$ MXene@Ni Microspheres. ACS Nano 16:1150–1159. https://doi.org/10.1021/acsnano.1c08957

55. Wang Y-Y, Zhu J-L, Li N et al (2022) Carbon aerogel microspheres with in-situ mineralized TiO$_2$ for efficient microwave absorption. Nano Res 15:7723–7730. https://doi.org/10.1007/s12274-022-4494-0

56. Qiang R, Du Y, Chen D et al (2016) Electromagnetic functionalized Co/C composites by in situ pyrolysis of metal-organic frameworks (ZIF-67). J Alloys Compd 681:384–393. https://doi.org/10.1016/j.jallcom.2016.04.225

57. Li S, Lin L, Yao L et al (2021) MOFs-derived Co-C@C hollow composites with high-performance electromagnetic wave absorption. J Alloys Compd. https://doi.org/10.1016/j.jallcom.2020.158183

58. Liu P, Gao S, Wang Y et al (2019) Core-shell CoNi@graphitic carbon decorated on B, N-codoped hollow carbon polyhedrons toward lightweight and high-efficiency microwave attenuation. ACS Appl Mater Interfaces 11:25624–25635. https://doi.org/10.1021/acsami.9b08525

59. Liu P, Gao S, Zhang G et al (2021) Hollow engineering to Co@N-doped carbon nanocages via synergistic protecting-etching strategy for ultrahigh microwave absorption. Adv Funct Mater. https://doi.org/10.1002/adfm.202102812

60. Wang Y, Xu J, He P et al (2023) Controlled-etching assisted fabrication of yolk-shell Co/C nanocubes with dual loss mechanisms to improve electromagnetic wave absorption abilities. J Alloys Compd. https://doi.org/10.1016/j.jallcom.2023.170017

61. Fang D, Liu S, Li J et al (2023) Absorber design based on In/C@Co/C composites for efficient microwave absorption. J Alloys Compd. https://doi.org/10.1016/j.jallcom.2023.170992

62. Chen X, Guo S, Tan S et al (2023) An environmentally friendly chitosan-derived VO$_2$/carbon aerogel for radar infrared compatible stealth. Carbon. https://doi.org/10.1016/j.carbon.2023.118313

63. Zhang R, Wang L, Xu C et al (2022) Vortex tuning magnetization configurations in porous Fe$_3$O$_4$ nanotube with wide microwave absorption frequency. Nano Res 15:6743–6750. https://doi.org/10.1007/s12274-022-4401-8

64. Li B, Tian H, Li L et al (2024) Graphene–assisted assembly of electrically and magnetically conductive ceramic nanofibrous aerogels enable multifunctionality. Adv Funct Mater. https://doi.org/10.1002/adfm.202314653

65. Li F, Wu N, Kimura H et al (2023) Initiating binary metal oxides microcubes electromagnetic wave absorber toward ultrabroad absorption bandwidth through Interfacial and defects modulation. Nano-Micro Lett. https://doi.org/10.1007/s40820-023-01197-0

66. Li F, Li Q, Kimura H et al (2023) Morphology controllable urchin-shaped bimetallic nickel-cobalt oxide/carbon composites with enhanced electromagnetic wave absorption performance. J Mater Sci Technol 148:250–259. https://doi.org/10.1016/j.jmst.2022.12.003

67. Guan X, Tan S, Wang L et al (2023) Electronic modulation strategy for mass-producible ultrastrong multifunctional biomass-based fiber aerogel devices: interfacial bridging. ACS Nano 17:20525–20536. https://doi.org/10.1021/acsnano.3c07300

68. Qiu J, Xin Z, Zhang M et al (2023) Facile synthesis of yolk-shell pompon-like Fe@void@CeO$_2$@Ni nanospheres with enhanced microwave absorption properties. Appl Surf Sci. https://doi.org/10.1016/j.apsusc.2022.155873

69. Li F, Bi Z, Kimura H et al (2023) Energy-and cost-efficient salt-assisted synthesis of nitrogen-doped porous carbon matrix decorated with nickel nanoparticles for superior electromagnetic wave absorption. Adv Compos Hybrid Mater. https://doi.org/10.1007/s42114-023-00710-8

70. Lin J, Qiao J, Tian H et al (2023) Ultralight, hierarchical metal-organic framework derivative/graphene hybrid aerogel for electromagnetic wave absorption. Adv Compos Hybrid Mater. https://doi.org/10.1007/s42114-023-00762-w

71. Zhao X, Li H, Zhang M et al (2022) Hierarchical nanocages assembled by NiCo-layered double hydroxide nanosheets for a high-performance hybrid supercapacitor. ACS Appl Mater Interfaces 14:34781–34792. https://doi.org/10.1021/acsami.2c08903

72. Zhang M, Qiu J, Xin Z et al (2021) In situ reduced multi-core yolk-shell Co@C nanospheres for broadband microwave absorption. Materials. https://doi.org/10.3390/ma14164610